BNL-225700-2024-JAAM

Amorphous-crystalline transition-driven synthesis of Co single-atom catalysts on MoO3 for enhanced hydrogen evolution in acidic and alkaline media

K. Kim, C. Nam

To be published in "Chemical Engineering Journal"

May 2024

Center for Functional Nanomaterials

Brookhaven National Laboratory

U.S. Department of Energy

USDOE Office of Science (SC), Basic Energy Sciences (BES). Scientific User Facilities (SUF)

Notice: This manuscript has been authored by employees of Brookhaven Science Associates, LLC under Contract No.DE-SC0012704 with the U.S. Department of Energy. The publisher by accepting the manuscript for publication acknowledges that the United States Government retains a non-exclusive, paid-up, irrevocable, world-wide license to publish or reproduce the published form of this manuscript, or allow others to do so, for United States Government purposes.

DISCLAIMER

This report was prepared as an account of work sponsored by an agency of the United States Government. Neither the United States Government nor any agency thereof, nor any of their employees, nor any of their contractors, subcontractors, or their employees, makes any warranty, express or implied, or assumes any legal liability or responsibility for the accuracy, completeness, or any third party's use or the results of such use of any information, apparatus, product, or process disclosed, or represents that its use would not infringe privately owned rights. Reference herein to any specific commercial product, process, or service by trade name, trademark, manufacturer, or otherwise, does not necessarily constitute or imply its endorsement, recommendation, or favoring by the United States Government or any agency thereof or its contractors or subcontractors. The views and opinions of authors expressed herein do not necessarily state or reflect those of the United States Government or any agency thereof.

Amorphous-crystalline transition-driven synthesis of Co single-atom catalysts on MoO_3 for enhanced hydrogen evolution in acidic and alkaline media

Kiwon Kim [b], Cheolho Kim [a], Seong-Min Bak [c], Chang-Yong Nam [d], Jun Hyuk Moon [a]

[a]Department of Chemical and Biological Engineering, School of Smart Mobility, Korea University, Seoul 02841, Republic of Korea

[b]Department of Chemical and Biomolecular Engineering, Sogang University, Seoul 04107, Republic of Korea

[c]Department of Materials Science and Engineering, Yonsei University, Seoul 03722, Republic of Korea

[d]Center for Functional Nanomaterials, Brookhaven National Laboratory, Upton, NY 11973, United States

Abstract

Single atom catalysts (SACs) dispersed in metal oxide supports offer not only maximized catalyst utilization but also extended modulation capabilities through interactions between the SA and its support. However, achieving facile preparation and ensuring electrochemical durability of such SACs, particularly for hydrogen evolution reaction (HER) applications, remain formidable challenges. Our study addresses these issues by employing an amorphous-to-crystalline phase transition in MoO_3 to synthesize a cobalt (Co) SA catalyst. This method facilitates the production of highly selective SA catalysts at low temperatures and ensures their enhanced stability in HER applications. The Co SA MoO_3 catalyst exhibits superior performance in HER, operating effectively in both acidic and alkaline environments. Significantly, it maintains stable HER activity across these diverse electrolytic conditions. Our Density Functional Theory (DFT) calculations provide insights into the exceptional HER performance of Co SA MoO_3. These calculations reveal that the strong affinity for hydrogen and water, facilitated by the modulation of the p-band orbitals at specific oxygen sites adjacent to the Co SA, establishes a thermoneutral pathway for HER. This study represents a pivotal advancement, showcasing a highly practical and robust single-atom catalyst, marking a significant stride towards sustainable energy solutions.

Keywords: Phase transition, P-band orbital, Terminal oxides, Hydrogen evolution reaction, Single atom catalyst

1. Introduction

The transition to a hydrogen-based energy system is a pivotal step towards achieving 'carbon neutrality' and fostering a sustainable environment [1], [2]. Hydrogen, as an energy carrier, boasts high storage and energy density and is notably free from the emission of carbon dioxide, a major greenhouse gas [3], [4]. The electrochemical hydrogen evolution reaction (HER) is increasingly garnering attention as an environmentally friendly method for hydrogen production [5], [6]. Yet, this process encounters the challenge of overcoming slow kinetics with high overpotential [2], [7]. More specifically, the Volmer step, which forms the hydrogen atom intermediate, exhibits a high energy barrier [8], [9]. Among the catalysts used in HER, Pt is the most efficient over a wide pH range; however, its high cost, limited availability, and concerns about long-term durability significantly impede its practical application [10], [11]. Therefore, there is a continuing demand for efficient and economical catalysts for the HER [6], [12].

Single-atom catalysts (SACs) are increasingly recognized as promising alternatives to noble metal catalysts for the HER [13], [14]. Their primary advantage is the efficient utilization of catalysts at the atomic level, where isolated SAs maximize catalytic activity [15], [16]. These catalysts also possess the unique ability to modulate their activity through interactions with heterogeneous supports, thereby offering additional control over their catalytic behaviour [17], [18]. The choice of support material is crucial for distributing

SAs and influencing their interaction with the support [19]. This aspect is not just pivotal for controlling the SA-support interactions but also plays a key role in anchoring SAs [20], [21], [22]. While carbon-based materials like graphene, amorphous carbon, and porous carbon have traditionally been widely employed, recent research has increasingly turned its attention to various metal compound supports. Examples of these supports include TiO_2, Fe_2O_3, NiO, CeO_2, MoS_2, Ni_3S_2, WS_2, $CoSe_2$, and NiSe [5], [6], [21], [23], [24], [25], [26], [27], [28].

Metal oxide supports, in particular, have garnered considerable attention due to their ability to offer robust metal–support interactions across a broad spectrum [8], [23]. Metal oxides possess excellent chemical/electrochemical stability and provide synergy as 'cocatalysts' with single-atom catalysts [29], [30]. Moreover, metal oxides provide a tunable and diverse route for synthesis [29], [30]. For example, Xu and coworkers have formed Pt SAs on amorphous MoO_x; they confirmed the strong interaction of Pt-O bonding and achieved an overpotential of 19 mV at 10 mA cm^{-2} in the application of the HER [31]. Hesnen and coworkers fabricated Pd single-atom catalysts on CeO_2 support for CO oxidation. They confirmed the stabilization of Pd that is readily reduced in CO oxidation by CeO_2 [27]. Wang and coworkers introduced single-atom Pt to NiO/Ni; this catalyst improved HER kinetics by lowering the water dissociation energy in alkaline conditions [26]. Tao and coworkers have formed Pt SAs by strong covalent metal–support interaction on Fe_2O_3 support; the Pt single-atom catalyst achieved a 4-fold improvement in methane conversion compared to Pt nanoparticles [32]. Despite these achievements, these approaches remain burdensome because they often require harsh chemical etching (e.g., reduction in a strong alkaline solution) or high-temperature heat treatment (e.g., thermal reduction at high temperatures > 900 °C) of the oxide support to enrich oxygen/transition metal vacancies or dangling/unsaturated edge sites for immobilization of SAs [28], [33], [34]. Consequently, the development of methods for the facile incorporation of SAs into oxide supports, along with ensuring their physicochemical stability within these oxides, still needs to be explored for the practical application of SA catalysts.

In this study, we present a novel synthetic route for Co SACs supported on MoO_3 by using the amorphous-to-crystalline transition of MoO_3 supports. Here, the loose atomic arrangement of the oxygen-deficient/unsaturated sites in amorphous MoO_3 selectively captures and chemically anchors single Co ions, while thermal crystallization incorporates Co SA atoms into the MoO_3 lattice. This method contrasts with the direct use of crystalline MoO_3 support to form SACs, which typically relies on the van der Waals forces of the MoO_3 interlayer or simply oxygen vacancy sites to anchor SAs (Table S1) [11], [35]. Additionally, our approach differs from the doping processes with MoO_3 by solution coprecipitation [36], where doping atoms are often included in the bulk rather than selectively on the support surface [37]. Moreover, coprecipitation is susceptible to forming clusters or even phase-separated doping atoms [37]. The Co SA MoO_3 catalyst exhibits excellent and stable HER activity in both acidic and alkaline electrolytes; a low overpotential of 87 mV and a low Tafel slope of 98 mV dec^{-1} at 10 mA cm^{-2} are achieved in a 1 M KOH electrolyte. In addition, a low overpotential of 112 mV and a low Tafel slope of 98 mV dec^{-1} are achieved at 10 mA cm^{-2} in a 0.5 M H_2SO_4 electrolyte. Furthermore, the Co SA MoO_3 catalyst maintains stable activity for at least 35 h in both electrolytes. The high HER activity in acidic and alkaline media was rationalized through density functional theory (DFT) calculations, which confirmed the enhanced adsorption for H^+ and H_2O on Co SA MoO_3, along with the thermoneutral Gibbs energy evolution for the HER.

2. Results and discussion

2.1. Synthesis of Co SA MoO_3

The fabrication of Co SA MoO_3 by the amorphous–crystalline phase transition of MoO_3 is depicted in Fig. 1**a**. First, oxygen-deficient amorphous MoO_3 is deposited on Ni foam by thermal evaporation in an argon atmosphere. A high-resolution TEM (HRTEM) image of the deposited MoO_3 shows a disordered, amorphous atomic arrangement (Fig. 1b). The inset image of selected area electron diffraction (SAED)

shows the halo ring pattern, which is a feature in the amorphous arrangement (Fig. 1b). Electron paramagnetic resonance (EPR) analysis of the deposited MoO_3 identifies the presence of oxygen vacancies at g = 1.999 and coordinatively unsaturated Mo^{5+} at g = 1.933 (Fig. S1) [35]. Next, Co^{2+} cations are adsorbed onto the deposited MoO_3 by immersion in 0.05 M $CoCl_2$ ethanol solution (see supplementary note #1). Here, the Co^{2+} cations can be trapped in a loose atomic arrangement with oxygen vacancies or coordinatively unsaturated. Specifically, the loose atomic arrangement restricts the accommodation of SAs of Co, and the depletion/unsaturated sites chemically anchor Co SAs (Fig. S2).

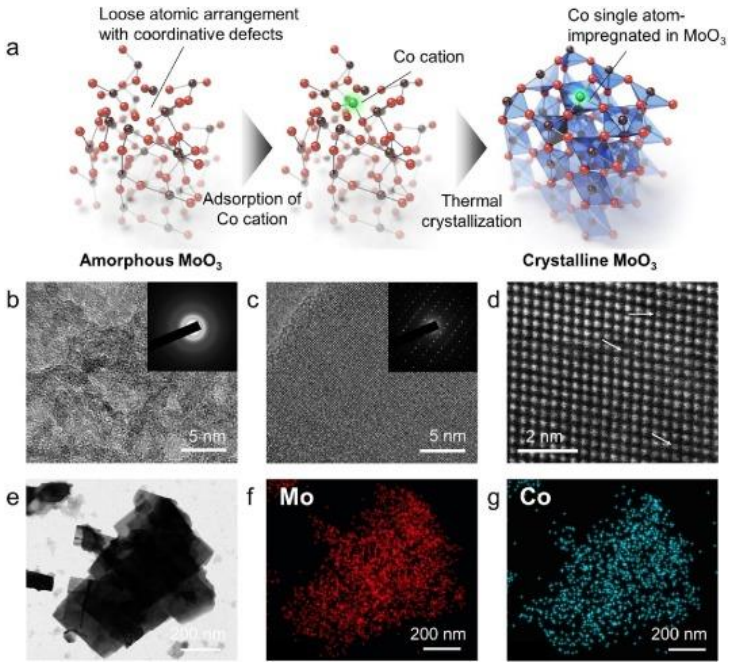

Fig. 1. **Preparation of Co SA MoO_3.** a) Scheme depicting the formation of single atoms of Co through the amorphous-to-crystalline transition of MoO_3. b) HRTEM image and SAED image (inset) of amorphous MoO_3. c) HR TEM image and SAED image of Co single-atom MoO_3 (inset). d) HAADF-STEM image of Co single-atom MoO_3; the arrows point to atoms with relatively dark contrast, which correspond to Co atoms. e-g) Low-resolution TEM images of Co single-atom MoO_3, Mo and Co mapped images, respectively.

In the final step, the Co^{2+}-adsorbed amorphous MoO_3 is subjected to low-temperature (420 °C) annealing in an ambient environment. This procedure induces an amorphous-to-crystalline phase transition accompanied by the oxidation of MoO_3. During this transition, the impregnated Co ions form chemical bonds within the lattice, resulting in the dispersion of single Co atoms throughout the MoO_3 matrix. (Fig. 1a). Post-heat treatment, the HRTEM image of MoO_3 clearly exhibits a crystalline phase. This is evidenced by lattice fringes corresponding to the (0 4 0) plane of crystallized MoO_3 with a d-spacing of 0.348 nm [29], along with the associated SAED pattern (Fig. 1c) [29]. However, the SAED pattern lacks diffraction spots characteristic of Co-based materials (e.g., oxides or metals), suggesting that Co is present as SAs. In the high-angle annular dark-field STEM (HAADF-STEM) image, individual dark spots of approximately 2 Å in size (Fig. 1d) are visible. Since Co is a lighter element than Mo, Co is observed with a darker contrast in the HAADF image [38], thus suggesting that these dark spots likely represent SAs of Co dispersed in MoO_3 (Fig. S3). The low-resolution TEM elemental mapping images of Co SA MoO_3 confirm the uniform dispersion of Co SAs (Fig. 1e-1g). The content of Co is approximately 2.4 wt%, as determined by inductively coupled plasma–atomic emission spectroscopy (ICP–AES) (Table S1). Remarkably, this content is higher than that in previous SA catalysts impregnated in oxide, such as 1 ~ 1.5 wt% for Pt SA

Fe_2O_3, 0.25 wt% for Au SA defective TiO_2 and 1.82 % for Co SA RuO_2 [28], [39], [40]. For comparison, we also prepare a sample where crystalline MoO_3 is first synthesized and subjected to Co^{2+} adsorption and heat treatment. This sample exhibited Co cluster particles approximately 30 nm in size (Fig. S4), with XRD analysis identifying these as Co oxide (Fig. S5). The results confirm that the heat treatment at 420 °C on crystalline MoO_3 does not lead to the doping or substitution of lattice elements by the adsorbed Co.

The change in chemical properties during thermal crystallization for Co SA MoO_3 formation was analyzed by X-ray diffraction (XRD) and X-ray photoemission spectroscopy (XPS). The XRD pattern of Co^{2+}-adsorbed amorphous MoO_3 does not exhibit any obvious peaks, indicating an amorphous feature (Fig. 2**a**). As the annealing temperature increases, the XRD pattern reveals the prominent peaks at 23.1°, 25.9°, and 27.6° (Fig. 2a). These peaks are attributed to the (1 1 0), (0 4 0), and (0 2 1) planes of orthorhombic MoO_3, respectively [29], [35]. The annealing temperature used in this study, 420 °C, effectively facilitates the amorphous-to-crystalline transition of MoO_3. Notably, the XRD pattern does not display any discernible Bragg peaks characteristic of Co oxide or metallic Co during the heat treatment. This absence of Co-related peaks signifies a high dispersion of Co SA within the matrix.

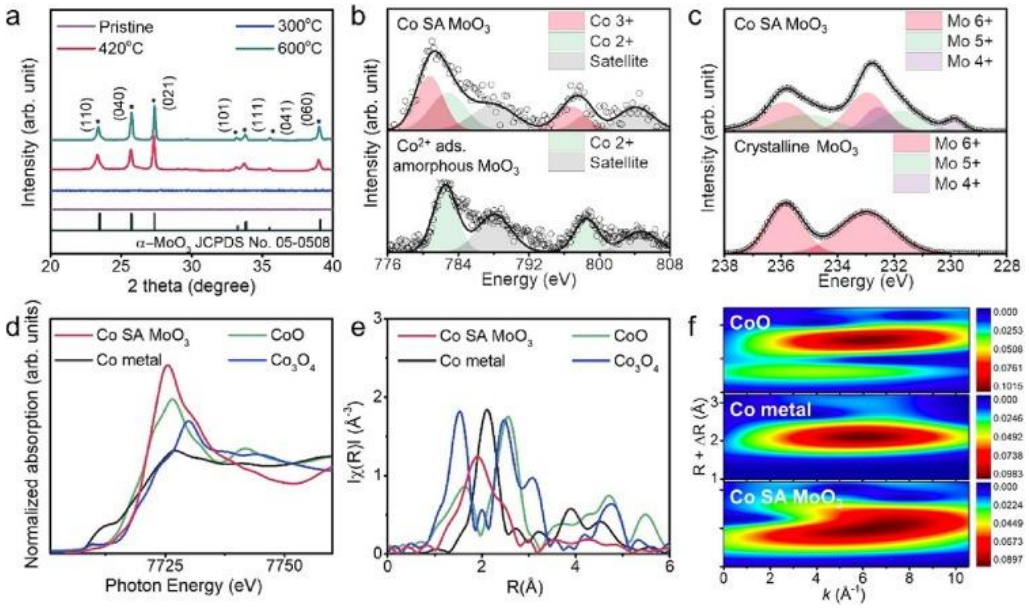

Fig. 2. **Chemical characterization.** a) XRD spectrum of Co^{2+} adsorbed amorphous MoO_3 (pristine) and the XRD spectra of this sample after undergoing heat treatment at various temperatures. b) Co 2p XPS profiles of Co^{2+}-adsorbed amorphous MoO_3 and Co SA MoO_3. c) Mo 3d XPS profiles of Co SA MoO_3 and crystalline MoO_3. d,e) Normalized XANES spectra and k^2-weighted FT EXAFS spectra of the Co K edge of Co SA MoO_3, Co metal, CoO and Co_3O_4. f) Wavelet transforms of Co SA MoO_3, Co metal, and CoO k^2-weighted Co K-edge EXAFS.

The Co 2p XPS spectra for Co SA MoO_3 and Co^{2+}-adsorbed amorphous MoO_3 are presented in Fig. 2b. The Co 2p spectrum exhibits two spin-orbital peaks, 2p 1/2 and 2p 3/2, associated with Co^{2+} and Co^{3+}, distinguished by peaks at 782.5/797.9 eV and 780.7/797.1 eV, with satellite peaks at 787.8/803.7 eV [39]. The spectrum of Co^{2+}-adsorbed amorphous MoO_3 mainly consists of peaks corresponding to Co^{2+}, confirming the adsorbed Co^{2+} as an ionic state. In contrast, Co SA MoO_3 shows an enhanced Co^{3+} peak, revealing the chemical bonding of Co^{2+} with MoO_3 during thermal oxidative crystallization. The Mo 3d XPS spectra of Co SA MoO_3 and crystallized MoO_3 without Co^{2+} treatment are compared in Fig. 2c. The Mo 3d spectrum is deconvoluted by peaks corresponding to Mo^{4+} (234.08 eV, 237. eV), Mo^{5+} (232.88 eV,

237.28 eV), and Mo^{6+} (232.3 eV, 235. eV) [29], [35]. The spectrum of crystalline MoO_3 exhibits Mo^{6+} dominant peaks, indicating MoO_3 formation by thermal oxidation. In contrast, the Co SA MoO_3 shows peaks of Mo^{4+} and Mo^{5+}, suggesting a difference in the oxidation states of Mo in the presence of Co^{2+}.

We use X-ray absorption near-edge structure (XANES) and extended X-ray absorption fine structure (EXAFS) to probe the electronic and local structure of Co in Co SA MoO_3. Co K-edge XANES spectra of Co SA MoO_3 and Co reference samples with Co metal, CoO and Co_3O_4 are presented in Fig. 2d. The absorption edge position of Co SA MoO_3 lies between the CoO and Co_3O_4 spectra, indicating that the Co valence of Co SA MoO_3 is between 2^+ and 2.67^+. This result aligns well with the Co 2p XPS result, which indicated the mixed valence of Co^{2+} and Co^{3+}. The Fourier-transformed (FT) k^2-weighted EXAFS spectra at Co K-edge for Co SA MoO_3 present a single prominent peak around 1.9 Å, distinct from Co-Co bonds (in Co metal: ~2 Å, in Co_3O_4 ~ 2.6 Å) or Co-O bonds (in Co_3O_4: ~1.7 Å) in the other Co references (Fig. 2e). This single peak EXAFS feature, without high shell peaks, is a characteristic feature of single-atom catalyst systems. Previously, Co SAs incorporated into Bi_3O_4Br exhibited a similar single strong peak without high shell peaks [41]. This peak correlates with the Co-O coordination in the first shell of Co SA MoO_3, suggesting that Co atoms are atomically dispersed in MoO_3. These results support the analysis of HAADF-STEM imaging. Additionally, the EXAFS spectrum spectrum of Co SA MoO_3 exhibits a shoulder feature near 2.5 Å, shorter than the Co–Co bonding length of Co_3O_4. Since this distance is not equal to that of Co-Co in Co metal, we presume that this feature represents a Co-Co interaction among the SAs incorporated in MoO_3 rather than Co cluster typical of Co metal. The Mo K-edge EXAFS fitting indicates that the single Mo atom in Co SA MoO_3 has a coordination number near 6 with the surrounding oxygen atoms, suggesting a substitutional replacement of Mo atoms by Co SAs. (Fig. S6).

To further confirm the SA characteristic, we also conducted wavelet transform (WT)-EXAFS, which can provide better visibility of EXAFS in both k and R spaces [7], [42]. The WT-EXAFS spectrum of Co SA MoO_3 reveals a peak with maximum intensity at 6.3 A^{-1}. This peak is distinctly different from the Co-Co scattering observed in metallic Co, which appears at 6.0 A^{-1}, and from the Co-O/Co scattering in CoO, which manifests at 4.0 (corresponding to Co-O) and 7.0 A^{-1} (corresponding to Co-Co) (Fig. 2f). This comparison further confirms the isolated character of Co as a SA within the catalyst.

2.2. HER activity of Co SA MoO_3

The electrocatalytic HER activity of Co SA MoO_3 was assessed in both acidic (0.5 M H_2SO_4) and alkaline (1 M KOH) environments using linear sweep voltammetry (LSV) (Fig. 3**a and 3b**). All LSV curves were corrected with background current and IR loss (Fig. S7) [7]. The areal mass loading of the Co SA MoO_3 electrode was controlled to be 0.8 mg cm^{-2} (Fig. S8). Graphite foil and saturated calomel electrodes were employed as counter and reference electrodes, respectively. The experiments were conducted at a scan rate of 10 mV s^{-1}, within an applied voltage range of −0.5–0 V vs. the reversible hydrogen electrode (RHE). The scan rate was 10 mV s^{-1}, and the applied voltage range was −0.5–0 V vs. the RHE. We compared Co SA MoO_3 with both the bare crystalline MoO_3 and Co cluster MoO_3, (prepared by adsorbing Co^{2+} onto crystalline MoO_3 followed by heat treatment).

The overpotential of Co SA MoO_3 is 112 mV and 87 mV in acidic conditions (0.5 M H_2SO_4) and alkaline media (1 M KOH), respectively, at a reference current density of −10 mA cm^{-2}. These values are significantly lower than those observed for Co cluster MoO_3 or bare MoO_3 under identical conditions, and they are also comparable to those of commercial Pt/C electrodes (Fig. S9). Specifically, in acidic media, the overpotential values for Co SA MoO_3 are only 46 % and 35 % of those for Co cluster MoO_3 and bare MoO_3, respectively. Similarly, in alkaline media, these values are 53 % and 47 % of those for Co cluster MoO_3 and bare MoO_3, respectively. It is evident that while MoO_3 exhibits relatively low HER activity, the incorporation of Co SA significantly enhances this activity. Moreover, the performance of Co SA

MoO_3 surpasses previous results for both Co SA electrocatalysts and Mo-based compound electrocatalysts (Table S3).

The Tafel plots for Co SA MoO_3, Co-cluster MoO_3 and bare MoO_3 are compared in Fig. 3c and 3d. In an acidic medium (0.5 M H_2SO_4), Co SA MoO_3 exhibits a single Tafel slop of 98 mV/dec in the overpotential range of 80–160 mV; this slope is much smaller than the 160 mV/dec for Co-cluster MoO_3 and 163 mV/dec for bare MoO_3. The kinetics of Co SA MoO_3 for the HER in an acidic medium are markedly enhanced. The Tafel slope of Co SA MoO_3 in an alkaline medium (1 M KOH) is 88 mV/dec in the overpotential range of 90–180 mV, exhibiting a smaller value than the 116 mV/dec of Co-cluster MoO_3 and 137 mV/dec of bare MoO_3. Co SA MoO_3 also reveals rapid kinetics for the HER in alkaline media. The fast HER kinetics of Co SA MoO_3 are further confirmed by electrochemical impedance spectroscopy (EIS). EIS measures the charge transfer resistance to the HER on the electrocatalyst surface. We fit the Nyquist curve to an equivalent circuit featuring a resistance element representing the charge transfer resistance (R_{ct}) (Fig. S10). The R_{ct} value (46 Ω) of Co SA MoO_3 is smaller than that of Co-cluster MoO_3 (92 Ω under acidic conditions, 64 Ω under alkaline conditions) or bare MoO_3 (136 Ω under acidic conditions, 90 Ω under alkaline conditions), indicating enhanced HER performance on Co SA MoO_3.

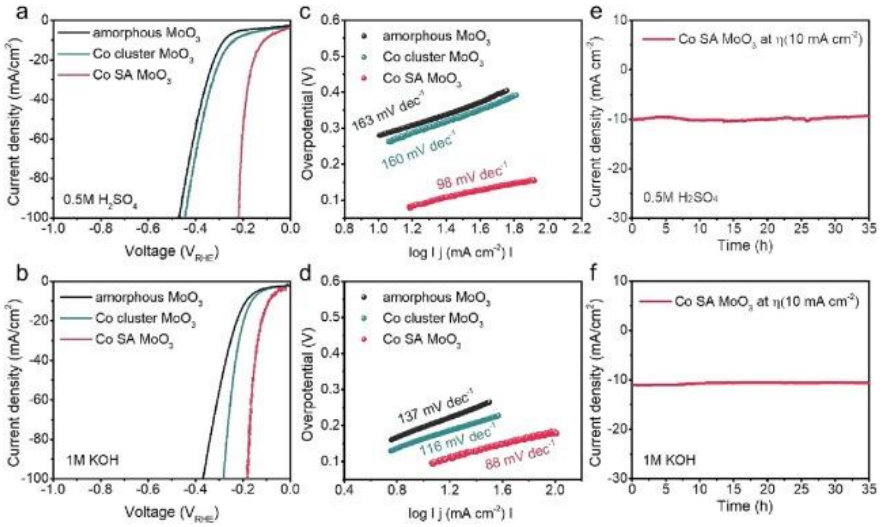

Fig. 3. **HER performance.** a,b) iR-corrected LSV curves and c,d) Tafel slopes of Co SA MoO_3, amorphous MoO_3, and Co cluster MoO_3. Long-term stability test of Co SA MoO_3 for 35 h at constant overpotentials of e) 98 mV and f) 88 mV. The electrolyte in a, c, and e) is 0.5 M H_2SO_4, and the electrolyte in b, d, and f) is 1 M KOH. The scan rate for a, b, c, and d is 10 mV s^{-1}.

The Tafel slope also provides information on the HER mechanism [8], [9]. Typical slope values of ~ 120 mV dec^{-1}, ~40 mV dec^{-1} and ~ 30 mV dec^{-1} are often associated with rate-limiting Volmer ($H_3O^+ + e^- + M \rightarrow M{-}H + H_2O$), Heyrovsky ($M{-}H + H_3O^+ + e^- \rightarrow H_2 + H_2O + M$) and Tafel ($2\,M{-}H \rightarrow H_2 + 2\,M$) steps, respectively [43]. A comparison of the slopes in both media immediately confirms that Co SA MoO_3 follows a different HER mechanism than Co cluster MoO_3 and bare MoO_3. The Tafel slope of Co SA MoO_3 corresponds to a value between those typical for the Volmer and Heyrovsky step-limited reactions [44]. This result reveals that the rate-determining process of the HER on Co SA MoO_3 is comparatively efficient compared to other steps, where the HER likely involves a Volmer step, a rate-limiting Heyrovsky step, and a fast Tafel step [45], [46].

The electrochemically active surface area (ECSA) of Co SA MoO_3 was determined using cyclic voltammetry. ECSA plays a pivotal role in evaluating the intrinsic properties of electrocatalysts, as it

quantifies the surface area that supports the adsorption and redox reactions of ions [47]. The ECSA correlates directly with the double-layer capacitance. (Fig. S11 and S12). In an acidic medium, the double-layer areal capacitance of Co SA MoO_3 reaches 26 mF cm^{-2}. This value is 1.5- and 1.3-fold higher than the capacitances of 17 mF cm^{-2} and 20 mF cm^{-2} of the bare MoO_3 and the Co cluster MoO_3 for comparison, respectively. Similarly, in an alkaline medium, the double-layer areal capacitance of Co SA MoO_3 is 71 mF cm^{-2}, surpassing the capacitances of 47 mF cm^{-2} and 53 mF cm^{-2} of MoO_3 and Co cluster MoO_3 by 2.6- and 2.2-fold respectively. The outstanding ECSA of Co SA MoO_3 reveals a high utilization of Co SAs, along with high activity at Co single-atom sites.

We estimated the turnover frequency (TOF) to evaluate the intrinsic activity of the Co SA MoO_3 electrocatalyst. This calculation assumes that every single Co atom serves as an active site. The TOF value of Co SA MoO_3 is 0.54 s^{-1} at 87 mV, which is higher than 0.17 s^{-1} in Co cluster MoO_3 and 0.13 s^{-1} in bare MoO_3. This value is comparable to previously achieved values for single-atom catalysts: 0.41 s^{-1} for Co-SAS/HOPNC at 100 mV, 0.101 s^{-1} for Co-NG, 0.39 s^{-1} for CoNx-C, 0.153 s^{-1} for Co-N-C and 0.35 s^{-1} for Pt SAs on vanadium nitride [7], [47], [48].

As a crucial metric for the practical application of electrocatalysts, the stability of Co SA MoO_3 for a long-term HER is evaluated in acidic and alkaline media. (Fig. 3e and 3f). The current density at a potential of 112 mV in acidic media or 87 mV in alkaline media was recorded over 35 hrs. Remarkably, the decrease in current density in acidic and alkaline media is as small as 6.4 and 3.2 %, respectively, indicating the high durability of Co SA MoO_3. In contrast, Co cluster MoO_3 shows a decrease in current density of 63 % for 35 h in an alkaline medium (Fig. S13). This observation, along with the noted Co dissolution (Fig. S14), suggests that the stability of Co SA MoO_3 is linked to the chemically stable integration of Co SAs within the MoO_3 lattice. The long-term operational stability of Co SA MoO_3 was further confirmed by LSV and EIS analysis (Fig. S15). After 35 hrs, the LSV curve closely resembled the initial curve, with a modest increase in overpotential of only 9.8 % in acidic media and 11 % in alkaline media (Table S3). Similarly, the R_{ct} values measured by EIS showed a mere 4 % increase in both acidic and alkaline media during the 35-hr operation. Furthermore, any SA dissolution is observed during stability test in both acidic and alkaline media (Fig. S16).

2.3. Elucidation of HER mechanisms in Co SA MoO_3

To rationalize the high HER activity of Co SA MoO_3, we present the binding energy and HER free energy diagram by density functional theory (DFT) calculations. MoO_3 is characterized by a layered structure in the [0 1 0] direction, with Mo atoms coordinating with three distinct oxygen types: terminal (*t*), asymmetric (*a*) and symmetric (*s*) oxygen [49]. (Fig. 4**a**) Our calculation utilized an orthorhombic MoO_3 (0 4 0) plane, incorporating Co-substituted Mo in MoO_3 for the atomic structure of Co SA MoO_3. The adsorption energies on Co SA MoO_3 and bare MoO_3 are compared in Fig. 4b (top panel). First, the adsorption energy for H^+ was assessed to gauge the HER activity in an acidic solution. For bare MoO_3, the adsorption energies at the O_t, O_a and O_s sites are calculated as −2.58, −2.24 and −2.19 eV, respectively, with the O_t site exhibiting the highest binding energy. This finding aligns with previous DFT studies, which attributed the higher binding at the O_t site to its proximity to the Fermi level and the lower spatial restrictions especially for the co-adsorption of 2H [49]. For Co SA MoO_3, the adsorption energy of these sites increases by 36 % on average compared to bare MoO_3. This notable increase in adsorption energy is attributed to the electron deficiency of Co relative to Mo. A comparison of the differential charge densities between bare MoO_3 and Co SA MoO_3 reveals a significant local increase in charge density around Co in the latter. This observation suggests an enhanced covalent bonding character for hydrogen in Co SA MoO_3 (Fig. 4e). These findings regarding H^+ adsorption further support the high HER activity of Co SA MoO_3 in an acidic solution.

The adsorption energies of H_2O on Co SA MoO_3 and bare MoO_3 are also compared in Fig. 4b. In alkaline solutions, the adsorption and subsequent dissociation of H_2O occur prior to the H^+ adsorption step [50]. Therefore, the adsorption energy of H_2O is closely linked to the HER activity of a catalyst in an alkaline

environments. For Co SA MoO_3, the calculated adsorption energies of H_2O at the O_t, O_a and O_s sites are −4.57, −2.93 and −3.58 eV, respectively. Similar to the adsorption behavior observed in H^+ adsorption, the O_t site emerges as the most favorable for adsorption. In comparison to bare MoO_3, Co SA MoO_3 demonstrates increased adsorption energy at the O_t sites. This increase is likely due to the greater suitability of the O_t site for accommodating the larger H_2O molecules.

This analysis of adsorption energy strongly suggests that Co SA MoO_3 exhibits high HER activity in both acidic and basic media. This enhanced activity is primarily attributed to the increased adsorption energy at each oxygen site (O_t, O_s, and O_a) of Co SA MoO_3. The underlying mechanism for this increase is elucidated by examining the p-band center positions at the O_t, O_s, and O_a orbitals, as derived from the Partial Density of States (PDOS). In the comparative analysis with MoO_3, it is observed that the p-band center positions at the oxygen sites in Co SA MoO_3 are closer to the Fermi level; this proximity to the Fermi level implies a stronger binding affinity for hydrogen at these oxygen sites in Co SA MoO_3 (Fig. 4c) [51], [52]. In Fig. 4d, a linear correlation is identified between the relative positions of the p-band center and the hydrogen adsorption capacity at the Fermi level.

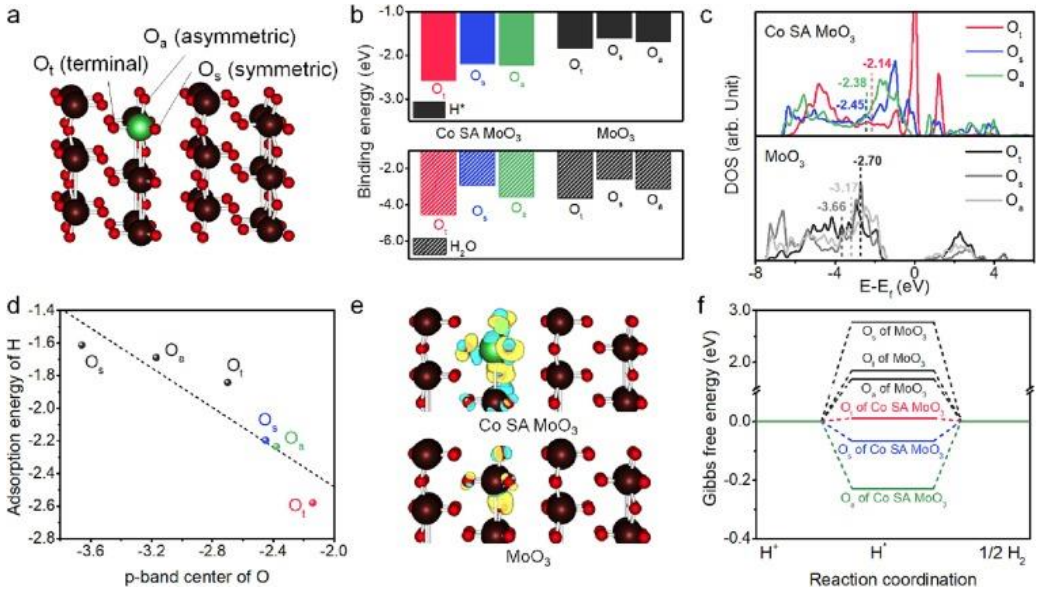

Fig. 4. **Reaction mechanism.** a) Optimized atomic structure of Co SA MoO_3, where Mo and O are colored black and red, respectively, and single-atom Co is colored green. Three oxygen positions are indicated: terminal (O_t), asymmetric (O_a), and symmetric (O_s). b) Calculated adsorption energies of H* and H_2O at three oxygen sites in MoO_3 and Co SA MoO_3. c) PDOS diagrams of the O_t, O_s, and O_a 2p orbitals in the Co SA MoO_3 and MoO_3, with dashed lines indicating the p-band center. d) Adsorption energy of hydrogen at the surface oxygen sites of Co SA MoO_3 and MoO_3, shown as a function of the O 2p-band center. e) Difference in charge density of Co SA MoO_3 and MoO_3. The isosurface value is set to 0.003 e $Å^{-3}$, with yellow and blue colors representing charge = accumulation and depletion. f) Free energy diagrams from DFT calculations for HERs at three oxygen sites on MoO_3 and Co SA MoO_3.

The Gibbs free energy (ΔG_{H^*}) for hydrogen adsorption serves as a descriptor for assessing HER catalytic activity. (Fig. 4d) For MoO_3, the ΔG_{H^*} values of the O_t, O_a and O_s sites are calculated to be 1.84, 1.68 and 2.77 eV, respectively. These large positive values indicate a significant energy barrier to the formation of H* intermediate, thus indicating an unfavorable HER in MoO_3. In contrast, the ΔG_{H^*} values for Co SA MoO_3 of the O_t, O_a and O_s sites are calculated as 0.01, −0.07 and −0.23 eV, respectively. The ΔG_{H^*} values of distorted Mo atom caused by near Co SA exhibits 0.84 (O_t), 0.75 (O_s) and 1.17 (O_a) eV, which is still

higher than those of Co SA MoO_3. (Fig. S17) Notably, the O_t and O_a sites of Co SA MoO_3 exhibit considerably lower ΔG_{H^*} values. This low energy barrier is indicative of facile hydrogen adsorption–desorption, aligning with the superior HER activity observed in Co SA MoO_3.

3. Conclusion

We employed the low-temperature amorphous-to-crystalline phase transition of MoO_3 to prepare a Co SA catalyst dispersed on a MoO_3 support. This method yields a stable Co SA atom chemically bound to the MoO_3 lattice. It involves accommodating SAs of Co cations within the loosely arranged, oxygen-deficient structure of amorphous MoO_3, followed by oxidative crystallization. XPS analysis validates the formation of a chemical bond between Co and MoO_3 during this phase transition. Additionally, XANES and EXAFS spectra confirm the successful impregnation of Co in MoO_3, demonstrating a uniform dispersion of Co SAs. Co SA MoO_3 exhibits excellent HER performance as an electrocatalyst in acidic and alkaline media. Notably, in an alkaline medium, the Co single-atom catalyst exhibits an overpotential of 87 mV and a current decay of only 3.2 % sustained over at least 35 hrs. In an acidic medium, the catalyst shows an overpotential of 112 mV and a current decay of only 6.4 % over 35 hrs. The overpotential value in alkaline media notably surpasses those of previous Co single-atom electrocatalysts and Mo compound electrocatalysts. Tafel slope analysis confirms a rate-limiting Heyrovsky step with rapid HER kinetics in Co SA MoO_3. Density Functional Theory (DFT) calculations provide insights into the adsorption and HER reaction energies at the O_t, O_a and O_s sites of Co SA MoO_3. The catalyst exhibits a high binding energy for water molecules and hydrogen ion adsorption, rationalizing the superior HER activity in acidic and alkaline media. Moreover, the free energy evolution of the HER presents a particularly thermoneutral profile for O_t and O_s of Co SA MoO_3, affirming the fast kinetics of the Co SA MoO_3 electrocatalyst at these sites. Our work demonstrates the potential of using amorphous-to-crystalline phase transitions to create stable and efficient single-atom catalysts for electrochemical applications.

4. Experimental section

Preparation of Co SA MoO_3: Amorphous MoO_3 is deposited on a Ni foam substrate by thermal evaporation. Thermal evaporation of MoO_3 was carried out at 50–55 W using a source of MoO_3 (99 % purity, 1–10 mm, Thailand). The deposition rate was controlled at 0.4 Å s^{-1}. The adsorption of Co ions was obtained by immersing an amorphous MoO_3 substrate in 0.15 M cobalt(II) chloride (98 %, Merck) ethanol solution for approximately 1 h. The Co^{2+}-adsorbed amorphous MoO_3 was sintered for 2 h at 420 °C at a ramping rate of 5 °C min^{-1} in air, resulting in Co SA-impregnated MoO_3 (Co SA MoO_3). To prepare Co cluster MoO_3 for comparison, we first heat-treated amorphous MoO_3 at 420 °C to obtain crystalline MoO_3, which adsorbed Co ions, followed by heat treatment at 420 °C.

Characterization: Field-emission scanning electron microscopy (FE-SEM) and TEM were performed on JSM-7100F (JEOL) and JEM-2100F (JEOL) scanning electron microscopes, respectively. Elemental analysis was performed using energy dispersive X-ray spectroscopy (EDXS) (Bruker, Xflash Detector 4010) in TEM. For crystal phase analysis, XRD (Davinci D8 Advance diffractometer, Cu Kα radiation) was used. The measurements were recorded at a scan rate of 0.03° s^{-1}. XPS was performed in a Leybold spectrometer with an Al Kα monochromatic beam (1486.6 eV) (150 W input power, ESCALAB250 XPS system, Theta Probe XPS system). Co K-edge x-ray absorption spectroscopy (XAS) was performed under ambient conditions in the Pohang Accelerator Laboratory (7D-XAFS beamline in PLS-II) equipped with a Si(1 1 1) crystal as a monochromator. The XANES and EXAFS data were handled and processed using the Demeter Software package. For each spectrum, the built-in AUTOBK algorithm was used to normalize the absorption coefficient, μ(k), and separate the χ(k) functions from the isolated atom absorption background. The extracted EXAFS signal, χ(k), was weighted by k2, and then Fourier transform (FT) was applied in k-ranges of 2.5–11 $Å^{-1}$, using the Hanning window function to obtain the magnitude plots of the EXAFS

spectra in R-space (Å). The FT peaks were not phase-corrected, and thus the actual bond lengths are approximately 0.2–0.4 Å longer. WT-EXAFS data were processed using the MATLAB program.

Electrochemical characterization: Electrochemical measurements were evaluated using a multichannel potentiostat/galvanostat (PARSTAT MC 1000) in a three-electrode system. A saturated calomel reference electrode (saturated KCl, Koslow Scientific Company, USA) was used as a reference electrode, and a graphite rod (6 mm diameter, WCCk1-GR002, Korea) was used as a counter electrode. Polarization curves were recorded at a scan rate of 5 mV s^{-1}. The potential measured with the reference electrode of the SCE was corrected with the RHE using the formula E(RHE) = E(SCE) + 0.241 + 0.059*pH. Chronopotentiometry was used to record changes in current at a fixed potential. EIS was performed with a 5 mV ac voltage amplitude in potentiostatic mode (VersaSTAT, Ametek) over a frequency range of 0.05–100 kHz. The EIS profile was made by Z-view software (Scribner Associates). TOF was obtained using TOF = J × S × μ/(2 × F × n), where J (A cm^{-2}) is the current density at a given potential (87 mV), S is the area of the electrode, F is the Faraday constant (96485C mol^{-1}), n is the number of moles of active sites on the electrode, and μ is the faradaic efficiency. C_{dl} for evaluating the electrochemical surface area (ECSA) was obtained by cyclic voltammetry. Specifically, C_{dl} is measured in cyclic voltammetry measurements at different scan rates from 0.230 to 0.325 V_{RHE} in 0.5 M H_2SO_4 and 1 M KOH solutions.

DFT calculations: DFT calculations were performed using the Quantum ESPRESSO package. The generalized gradient approximation (GGA) functional of Perdew–Burke–Ernzerhof (PBE) was applied for the exchange–correlation potential. The vdW interaction was corrected using DFT-D3. For the plane-wave basis set, the kinetic energy cut off of the wave functions was set to 50 eV, and the kinetic energy cut off of the charge density was set to 450 eV. For Monkhorst–Pack meshes, a 3 × 3 × 3 k-point mesh was applied, and a vacuum spacing of 15 Å was applied on the (0 1 0) surface. The adsorption energy of hydrogen was calculated using the following formula: $E_B = E(H + sub) - E(4H_2)*0.125 - E(sub)$, where $E(H + sub)$, $E(4H_2)$*0.125 and $E(sub)$ represent the energies of the hydrogen adsorbed system, hydrogen and substrate, respectively. The p-band center is calculated by the formula: $\varepsilon p = \int_{-\infty}^{E_f} E\rho p(E)dE / \int_{-\infty}^{E_f} \rho p(E)dE$, where ρp represents the density of states projected on atomic oxygen p band and E_f is the Fermi level. The Gibbs energy was calculated by the following formula: $\Delta G = \Delta E_{DFT} + \Delta E_{ZPE} - T\Delta S - n_e U + \Delta G_{pH.}$, where ΔE_{DFT} is the electronic energy difference, ΔE_{ZPE} is the zero-point energy difference, and ΔS is the entropy change. N_e and U represent the number of electrons transferred and the applied bias, respectively. ΔG_{pH} corresponds to the correction by the pH.

Authorship contribution statement

Kiwon Kim: Investigation, Formal analysis. Cheolho Kim: Writing – review & editing, Validation. Seong-Min Bak: Validation, Formal analysis. Chang-Yong Nam: Writing – review & editing, Validation. Jun Hyuk Moon: Writing – review & editing, Writing – original draft, Supervision, Project administration, Funding acquisition.

Declaration of competing interest

The authors declare that they have no known competing financial interests or personal relationships that could have appeared to influence the work reported in this paper.

Acknowledgements

J.H.M acknowledge the use of the resources of Pohang Accelerator Laboratory (PAL) and also the support from the National Research Foundation of Korea (grant no. 2021M3D3A1A01022112). C.-Y.N.

acknowledge the use of the resources of the Center for Functional Nanomaterials (CFN), which is U.S. Department of Energy (DOE) office of Science User Facilities at Brookhaven National Laboratory under Contract No. DE-SC0012704.

References

1. D.I. Jeong, H.W. Choi, S. Woo, J.H. Yoo, D. Kang, S. Kim, B. Lim, J.H. Kim, S.-W. Kim, B.K. Kang
   Electronic structure modification and N-doped carbon shell nanoarchitectonics of Ni_3FeN@ NC for overall water splitting performance evaluation
   J. Mater. Chem. A, 10 (2022), pp. 16704-16713, 10.1039/D2TA04817E
2. Y. Wang, X. Li, M. Zhang, J. Zhang, Z. Chen, X. Zheng, Z. Tian, N. Zhao, X. Han, K. Zaghib
   Highly active and durable single-atom tungsten-doped $NiS_{0.5}Se_{0.5}$ nanosheet@ $NiS_{0.5}Se_{0.5}$ nanorod heterostructures for water splitting
   Adv. Mater., 34 (2022), p. 2107053, 10.1002/adma.202107053
3. C. Cai, K. Liu, Y. Zhu, P. Li, Q. Wang, B. Liu, S. Chen, H. Li, L. Zhu, H. Li
   Optimizing hydrogen binding on ru sites with RuCo alloy nanosheets for efficient alkaline hydrogen evolution
   Angew. Chem., 134 (2022), p. e202113664
4. A. Kumar, V.Q. Bui, J. Lee, A.R. Jadhav, Y. Hwang, M.G. Kim, Y. Kawazoe, H. Lee
   Modulating interfacial charge density of NiP_2–FeP_2 via coupling with metallic cu for accelerating alkaline hydrogen evolution
   ACS Energy Lett., 6 (2021), pp. 354-363, 10.1021/acsenergylett.0c02498
5. J.-D. Yi, R. Xu, G.-L. Chai, T. Zhang, K. Zang, B. Nan, H. Lin, Y.-L. Liang, J. Lv, J. Luo
   Cobalt single-atoms anchored on porphyrinic triazine-based frameworks as bifunctional electrocatalysts for oxygen reduction and hydrogen evolution reactions
   J. Mater. Chem. A, 7 (2019), pp. 1252-1259, 10.1039/C8TA09490J
6. M.D. Hossain, Z. Liu, M. Zhuang, X. Yan, G.L. Xu, C.A. Gadre, A. Tyagi, I.H. Abidi, C.J. Sun, H. Wong
   Rational design of graphene-supported single atom catalysts for hydrogen evolution reaction
   Adv. Energy Mater., 9 (2019), p. 1803689, 10.1002/aenm.201803689
7. R. Liu, Z. Gong, J. Liu, J. Dong, J. Liao, H. Liu, H. Huang, J. Liu, M. Yan, K. Huang
   Design of Aligned Porous Carbon Films with single-atom Co–N–C sites for high-current-density hydrogen generation
   Adv. Mater., 33 (2021), p. 2103533, 10.1002/adma.202103533
8. J. Huang, J. Han, T. Wu, K. Feng, T. Yao, X. Wang, S. Liu, J. Zhong, Z. Zhang, Y. Zhang
   Boosting hydrogen transfer during volmer reaction at oxides/metal nanocomposites for efficient alkaline hydrogen evolution
   ACS Energy Lett., 4 (2019), pp. 3002-3010, 10.1021/acsenergylett.9b02359
9. L. Wang, C. Lin, D. Huang, J. Chen, L. Jiang, M. Wang, L. Chi, L. Shi, J. Jin
   Optimizing the Volmer step by single-layer nickel hydroxide nanosheets in hydrogen evolution reaction of platinum
   ACS Catal., 5 (2015), pp. 3801-3806, 10.1021/cs501835c
10. S.H. Joo, S.J. Choi, I. Oh, J. Kwak, Z. Liu, O. Terasaki, R. Ryoo
    Ordered nanoporous arrays of carbon supporting high dispersions of platinum nanoparticles
    Nature, 412 (2001), pp. 169-172, 10.1038/35084046
11. B. Conway, B. Tilak
    Interfacial processes involving electrocatalytic evolution and oxidation of H_2, and the role of chemisorbed H
    Electrochim. Acta, 47 (2002), pp. 3571-3594, 10.1016/S0013-4686(02)00329-8
12. K. Huang, Z. Wei, J. Liu, Z. Gong, J. Liu, M. Yan, G. He, H. Gong, Y. Hu, Y. He

Engineering the morphology and microenvironment of a graphene-supported co-N-C single-atom electrocatalyst for enhanced hydrogen evolution
Small, 18 (2022), p. 2201139, 10.1002/smll.202201139
13. Y. Chen, S. Ji, C. Chen, Q. Peng, D. Wang, Y. Li
Single-atom catalysts: synthetic strategies and electrochemical applications
Joule, 2 (2018), pp. 1242-1264, 10.1016/j.joule.2018.06.019
14. A. Alarawi, V. Ramalingam, J.-H. He
Recent advances in emerging single atom confined two-dimensional materials for water splitting applications
Mate. Today Energy, 11 (2019), pp. 1-23, 10.1016/j.mtener.2018.10.014
15. S. Ye, F. Luo, Q. Zhang, P. Zhang, T. Xu, Q. Wang, D. He, L. Guo, Y. Zhang, C. He
Highly stable single pt atomic sites anchored on aniline-stacked graphene for hydrogen evolution reaction
Energy Environ. Sci., 12 (2019), pp. 1000-1007, 10.1039/C8EE02888E
16. D. Liu, X. Li, S. Chen, H. Yan, C. Wang, C. Wu, Y.A. Haleem, S. Duan, J. Lu, B. Ge
Atomically dispersed platinum supported on curved carbon supports for efficient electrocatalytic hydrogen evolution
Nat. Energy, 4 (2019), pp. 512-518, 10.1038/s41560-019-0402-6
17. D.J. Cole-Hamilton
Homogeneous catalysis–new approaches to catalyst separation, recovery, and recycling
Science, 299 (2003), pp. 1702-1706, 10.1126/science.1081881
18. H. Zhang, W. Zhou, T. Chen, B.Y. Guan, Z. Li, X.W.D. Lou
A modular strategy for decorating isolated cobalt atoms into multichannel carbon matrix for electrocatalytic oxygen reduction
Energy Environ. Sci., 11 (2018), pp. 1980-1984, 10.1039/C8EE00901E
19. J. Liu
Catalysis by supported single metal atoms
ACS Catal., 7 (2017), pp. 34-59, 10.1021/acscatal.6b01534
20. H. Yan, H. Cheng, H. Yi, Y. Lin, T. Yao, C. Wang, J. Li, S. Wei, J. Lu
Single-atom Pd1/graphene catalyst achieved by atomic layer deposition: remarkable performance in selective hydrogenation of 1, 3-butadiene
J. Am. Chem. Soc., 137 (2015), pp. 10484-10487, 10.1021/jacs.5b06485
21. H. Zhang, J. Wei, J. Dong, G. Liu, L. Shi, P. An, G. Zhao, J. Kong, X. Wang, X. Meng
Efficient visible-light-driven carbon dioxide reduction by a single-atom implanted metal–organic framework
Angew. Chem., 128 (2016), pp. 14522-14526, 10.1002/anie.201608597
22. H. Zhang, G. Liu, L. Shi, J. Ye
Single-atom catalysts: emerging multifunctional materials in heterogeneous catalysis
Adv. Energy Mater., 8 (2018), p. 1701343, 10.1002/aenm.201701343
23. H. Wei, X. Liu, A. Wang, L. Zhang, B. Qiao, X. Yang, Y. Huang, S. Miao, J. Liu, T. Zhang
FeO_x-supported platinum single-atom and pseudo-single-atom catalysts for chemoselective hydrogenation of functionalized nitroarenes
Nat. Commun., 5 (2014), pp. 1-8, 10.1038/ncomms6634
24. E. Meza, R.E. Diaz, C.W. Li
Solution-phase activation and functionalization of colloidal WS_2 nanosheets with Ni single atoms
ACS Nano, 14 (2020), pp. 2238-2247, 10.1021/acsnano.9b09245
25. W. Yang, S. Zhang, Q. Chen, C. Zhang, Y. Wei, H. Jiang, Y. Lin, M. Zhao, Q. He, X. Wang
Conversion of intercalated MoO_3 to multi-heteroatoms-doped MoS_2 with high hydrogen evolution activity
Adv. Mater., 32 (2020), p. 2001167, 10.1002/adma.202001167
26. K.L. Zhou, Z. Wang, C.B. Han, X. Ke, C. Wang, Y. Jin, Q. Zhang, J. Liu, H. Wang, H. Yan

Platinum single-atom catalyst coupled with transition metal/metal oxide heterostructure for accelerating alkaline hydrogen evolution reaction
Nat. Commun., 12 (2021), pp. 1-10, 10.1038/s41467-021-24079-8
27. V. Muravev, G. Spezzati, Y.-Q. Su, A. Parastaev, F.-K. Chiang, A. Longo, C. Escudero, N. Kosinov, E.J. Hensen
Interface dynamics of Pd–CeO_2 single-atom catalysts during CO oxidation
Nat. Catal., 4 (2021), pp. 469-478, 10.1038/s41929-021-00621-1
28. J. Wan, W. Chen, C. Jia, L. Zheng, J. Dong, X. Zheng, Y. Wang, W. Yan, C. Chen, Q. Peng
Defect effects on TiO_2 nanosheets: stabilizing single atomic site Au and promoting catalytic properties
Adv. Mater., 30 (2018), p. 1705369, 10.1002/adma.201705369
29. Z. Luo, R. Miao, T.D. Huan, I.M. Mosa, A.S. Poyraz, W. Zhong, J.E. Cloud, D.A. Kriz, S. Thanneeru , J. He
Mesoporous MoO_{3-x} material as an efficient electrocatalyst for hydrogen evolution reactions
Adv. Energy Mater., 6 (2016), p. 1600528, 10.1002/aenm.201600528
30. F. Dvořák, M. Farnesi Camellone, A. Tovt, N.-D. Tran, F.R. Negreiros, M. Vorokhta, T. Skála, I. Matolínová, J. Mysliveček, V. Matolín
Creating single-atom pt-ceria catalysts by surface step decoration
Nat. Commun., 7 (2016), pp. 1-8, 10.1038/ncomms10801
31. J. Xu, C. Zhang, H. Liu, J. Sun, R. Xie, Y. Qiu, F. Lü, Y. Liu, L. Zhuo, X. Liu
Amorphous MoO_X-stabilized single platinum atoms with ultrahigh mass activity for acidic hydrogen evolution
Nano Energy, 70 (2020), Article 104529, 10.1016/j.nanoen.2020.104529
32. Y. Ren, Y. Tang, L. Zhang, X. Liu, L. Li, S. Miao, D. Sheng Su, A. Wang, J. Li, T. Zhang
Unraveling the coordination structure-performance relationship in Pt1/Fe2O3 single-atom catalyst
Nat. Commun., 10 (2019), pp. 1-9, 10.1038/s41467-019-12459-0
33. P. Zhai, M. Xia, Y. Wu, G. Zhang, J. Gao, B. Zhang, S. Cao, Y. Zhang, Z. Li, Z. Fan
Engineering single-atomic ruthenium catalytic sites on defective nickel-iron layered double hydroxide for overall water splitting
Nat. Commun., 12 (2021), pp. 1-11, 10.1038/s41467-021-24828-9
34. B.-H. Lee, S. Park, M. Kim, A.K. Sinha, S.C. Lee, E. Jung, W.J. Chang, K.-S. Lee, J.H. Kim, S.-P. Cho
Reversible and cooperative photoactivation of single-atom Cu/TiO_2 photocatalysts
Nat. Mater., 18 (2019), pp. 620-626, 10.1038/s41563-019-0344-1
35. W. Liu, C. Li, Q. Xu, P. Yan, C. Niu, Y. Shen, P. Yuan, Y. Jia
Anderson localization in 2D amorphous MoO_{3-x} monolayers for electrochemical ammonia synthesis
ChemCatChem, 11 (2019), pp. 5412-5416, 10.1002/cctc.201901171
36. H. Xian, H. Guo, J. Xia, Q. Chen, Y. Luo, R. Song, T. Li, E. Traversa
Iron-doped MoO3 nanosheets for boosting nitrogen fixation to ammonia at ambient conditions
ACS Appl. Mater. Interfaces, 13 (2021), pp. 7142-7151, 10.1021/acsami.0c19644
37. K. Maiti, N.H. Kim, J.H. Lee
Strongly stabilized integrated bimetallic oxide of Fe2O3-MoO3 Nano-crystal entrapped N-doped graphene as a superior oxygen reduction reaction electrocatalyst
Chem. Eng. J., 410 (2021), Article 128358, 10.1016/j.cej.2020.128358
38. J. Bai, J. Mei, T. Liao, Q. Sun, Z.G. Chen, Z. Sun
Molybdenum-promoted Surface reconstruction in polymorphic cobalt for initiating rapid oxygen evolution
Adv. Energy Mater., 12 (2022), p. 2103247, 10.1002/aenm.202103247
39. K. Shah, R. Dai, M. Mateen, Z. Hassan, Z. Zhuang, C. Liu, M. Israr, W.C. Cheong, B. Hu, R. Tu
Cobalt single atom incorporated in ruthenium oxide sphere: a robust bifunctional electrocatalyst for HER and OER

Angew. Chem., 134 (2022), p. e202114951
40. R. Lang, W. Xi, J.-C. Liu, Y.-T. Cui, T. Li, A.F. Lee, F. Chen, Y. Chen, L. Li, L. Li
Non defect-stabilized thermally stable single-atom catalyst
Nat. Commun., 10 (2019), pp. 1-10, 10.1038/s41467-018-08136-3
41. J. Di, C. Chen, S.-Z. Yang, S. Chen, M. Duan, J. Xiong, C. Zhu, R. Long, W. Hao, Z. Chi
Isolated single atom cobalt in Bi_3O_4Br atomic layers to trigger efficient CO_2 photoreduction
Nat. Commun., 10 (2019), pp. 1-7, 10.1038/s41467-019-10392-w
42. J. He, N. Li, Z.G. Li, M. Zhong, Z.X. Fu, M. Liu, J.C. Yin, Z. Shen, W. Li, J. Zhang
Strategic defect engineering of metal-organic frameworks for optimizing the fabrication of single-atom catalysts
Adv. Funct. Mater., 31 (2021), p. 2103597, 10.1002/adfm.202103597
43. J. Wei, M. Zhou, A. Long, Y. Xue, H. Liao, C. Wei, Z.J. Xu
Heterostructured electrocatalysts for hydrogen evolution reaction under alkaline conditions
Nanomicro Lett., 10 (2018), pp. 1-15, 10.1007/s40820-018-0229-x
44. T. Shinagawa, A.T. Garcia-Esparza, K. Takanabe
Insight on tafel slopes from a microkinetic analysis of aqueous electrocatalysis for energy conversion
Sci. Rep., 5 (2015), pp. 1-21, 10.1038/srep13801
45. A. Alobaid, C. Wang, R.A. Adomaitis
Mechanism and kinetics of HER and OER on NiFe LDH films in an alkaline electrolyte
J. Electrochem. Soc., 165 (2018), p. J3395, 10.1149/2.0481815jes
46. F. Bao, E. Kemppainen, I. Dorbandt, R. Bors, F. Xi, R. Schlatmann, R. van de Krol, S. Calnan
Understanding the hydrogen evolution reaction kinetics of electrodeposited nickel-molybdenum in acidic, Near-neutral, and alkaline conditions
ChemElectroChem, 8 (2021), pp. 195-208, 10.1002/celc.202001436
47. L. Wu, J.P. Hofmann
Comparing the intrinsic HER activity of transition metal dichalcogenides: pitfalls and suggestions
ACS Energy Lett., 6 (2021), pp. 2619-2625, 10.1021/acsenergylett.1c00912
48. M. Ma, X. Cheng, Z. Shi, C. Zhang, Y. Li, Y. Yang, C. Gong, Z. Zhang, H. Fei, C. Zhu
Role of N in transition-metal-nitrides for anchoring platinum-group metal atoms toward single-atom catalysis, small
Methods (2022), p. 2200295, 10.1002/smtd.202200295
49. Y.-H. Lei, Z.-X. Chen
DFT+ U study of properties of MoO3 and hydrogen adsorption on MoO3 (010)
J. Phys. Chem. C, 116 (2012), pp. 25757-25764, 10.1021/jp304122n
50. N. Mahmood, Y. Yao, J.W. Zhang, L. Pan, X. Zhang, J.J. Zou
Electrocatalysts for hydrogen evolution in alkaline electrolytes: mechanisms, challenges, and prospective solutions
Adv. Sci., 5 (2018), p. 1700464, 10.1002/advs.201700464
51. L. Giordano, K. Akkiraju, R. Jacobs, D. Vivona, D. Morgan, Y. Shao-Horn
Electronic structure-based descriptors for oxide properties and functions
Acc. Chem. Res., 55 (2022), pp. 298-308, 10.1021/acs.accounts.1c00509
52. B. Xing, G.-C. Wang
Insight into the general rule for the activation of the X-H bonds (X = C, N, O, S) induced by chemisorbed oxygen atoms
Phys. Chem. Chem. Phys., 16 (2014), pp. 2621-2629, 10.1039/c3cp53801j